INTERFACE

royalsocietypublishing.org/journal/rsif

Research

Cite this article: Dvoriashyna M, Foss AJE, Gaffney EA, Repetto R. 2020 Fluid and solute transport across the retinal pigment epithelium: a theoretical model. *J. R. Soc. Interface* **17**: 20190735.
http://dx.doi.org/10.1098/rsif.2019.0735

Received: 28 October 2019
Accepted: 10 January 2020

**Subject Category:**
Life Sciences–Mathematics interface

**Subject Areas:**
biomechanics, biophysics, biomathematics

**Keywords:**
retinal pigment epithelium, ion transport, fluid transport across epithelia

**Author for correspondence:**
Mariia Dvoriashyna
e-mail: dvoriashyna@damtp.cam.ac.uk

Electronic supplementary material is available online at https://doi.org/10.6084/m9.figshare.c.4823412.

THE ROYAL SOCIETY PUBLISHING

# Fluid and solute transport across the retinal pigment epithelium: a theoretical model

Mariia Dvoriashyna[1], Alexander J. E. Foss[2], Eamonn A. Gaffney[3] and Rodolfo Repetto[4]

[1]Department of Applied Mathematics and Theoretical Physics, University of Cambridge, Cambridge CB3 0WA, UK
[2]Department of Ophthalmology, Nottingham University Hospitals NHS Trust, Nottingham NG5 1PB, UK
[3]Wolfson Centre for Mathematical Biology, Mathematical Institute, University of Oxford, Oxford OX2 6GG, UK
[4]Department of Civil, Chemical and Environmental Engineering, University of Genoa, Via Montallegro 1, Genoa 16145, Italy

MD, 0000-0002-6057-1919; AJEF, 0000-0001-9649-0072; EAG, 0000-0002-6888-4362; RR, 0000-0001-9332-5063

The retina is composed of two main layers—the neuroretina and the retinal pigment epithelium (RPE)—that are separated by a potential gap termed the sub-retinal space (SRS). Accumulation of fluid in the SRS may result in a retinal detachment. A key function of the RPE is to prevent fluid accumulation in the SRS by actively pumping fluid from this space to the choroid. We have developed a mathematical model of this process that incorporates the transport of seven chemical species: $Na^+$, $K^+$, $Cl^-$, $HCO_3^-$, $H^+$, $CO_2$ and $H_2CO_3$. This allows us to estimate solute and water fluxes and to understand the role of the different membrane ion channels. We have performed a global sensitivity analysis using the extended Fourier amplitude sensitivity test to investigate the relative importance of parameters in generating the model outputs. The model predicts that flow across the RPE is driven by an osmotic gradient in the cleft gap between adjacent cells. Moreover, the model estimates how water flux is modified in response to inhibition of membrane ion channels and carbonic anhydrase (CA). It provides a possible explanation for how CA inhibitors, which are used clinically to prevent fluid accumulation in the SRS, may be acting.

## 1. Introduction

The retina is composed of two main layers—the neuroretina and the retinal pigment epithelium (RPE)—that are separated by a potential space termed the sub-retinal space (SRS). The RPE sits on a connective tissue layer called Bruch's membrane, below which is the choroid. The RPE is bounded above (the apical surface) by the SRS and below by the choroidal space, as shown in figure 1. The RPE cells themselves are coupled by tight junctions and this layer constitutes the outer blood–retinal barrier.

The photoreceptors face the apical surface of the RPE. The functions of the RPE include pumping fluid from the SRS to the choroid and transporting the carbon dioxide produced by the retina, and particularly by the photoreceptors, to the choroid, where it can be eliminated [1].

In a healthy retina, the RPE actively pumps fluid from the SRS to the choroid at a rate of about 4–10 $\mu l\, h^{-1}\, cm^{-2}$ [2,3]. It is a failure of this pumping that can lead to fluid accumulation in the SRS, which is associated with a number of pathological conditions, including serous retinal detachment, age-related macular degeneration and diabetic retinopathy [4]. The aim of this model is to understand how this fluid transport occurs.

The fluid transport is isotonic (i.e. without a significant difference in osmolarity between the apical and basal regions) and the standard explanation is that 'water follows the ions', i.e. water transport occurs in the main direction of ion

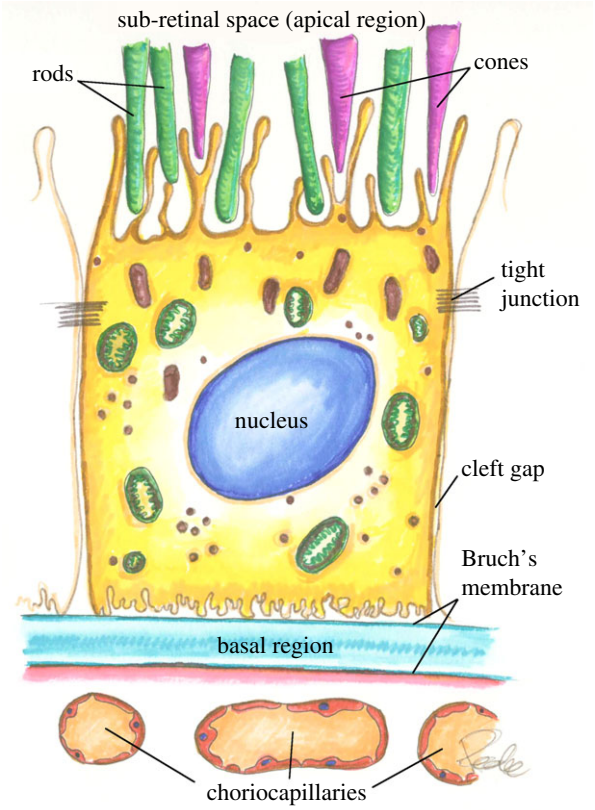


**Figure 1.** Sketch of the retinal pigment epithelium cell. Drawing by Prof. Federica Grillo (University of Genoa, Italy). (Online version in colour.)

transport [5]. However, the physical mechanisms behind this coupling are obscure.

A number of mathematical models have been developed to study isotonic fluid transport by epithelia. Diamond & Bossert [6] first proposed what is known as the standing gradient osmotic flow (or local osmosis) model. This model postulates the presence of an osmolarity gradient that is generated in the cleft gap between two adjacent cells. This gradient is generated by the active pumping of ions and it drives fluid into and along the cleft, resulting in transepithelial water transport. This model has been extended and applied to study isotonic water transport in a number of epithelia (e.g. [7–10]).

Electro-osmosis has been proposed as an alternative mechanism. It occurs as a result of the interaction of an electric field with non-zero spatial charge density that forms in a thin region close to the cell membrane. We previously developed a mathematical model that couples water and ion flow across the RPE that incorporates both local and electro-osmotic effects [11], allowing the investigation of the relative importance of these two possible mechanisms for fluid transport. This model looked at the presence of three different species: sodium ($Na^+$), potassium ($K^+$) and chloride ($Cl^-$). The model predicted that local osmosis, driven by the osmolarity gradient in the cleft gap, is comparable to the experimentally measured values of the flow and extensively dominates electro-osmosis.

However, that model had a number of limitations and the objective of this work is to extend the work in [11] to include the role of bicarbonate ($HCO_3^-$), carbon dioxide ($CO_2$), carbonic acid ($H_2CO_3$) and protons ($H^+$) along with the relevant ion channels, as they are thought to play an important role in fluid transport [12], with the aim of generating a more accurate quantitative estimate of transepithelial water and ion fluxes. Adding $HCO_3^-$ to our model is essential if one wants to describe physiological ion fluxes in detail. In our previous model, the $Na^+$ flux across the RPE was imposed to be zero. The addition of these extra species now allows the sodium flux to be modelled.

The importance of $CO_2$ and bicarbonate in fluid transport is shown by the enhancement of fluid flow by carbonic anhydrase (CA) inhibitors [13,14]. The enzyme CA catalyses the conversion of $CO_2$ and $H_2O$ to carbonic acid ($H_2CO_3$) and it is well known that some patients with macular oedema will respond to CA inhibition [15,16]. Adijanto *et al*. [1] conducted *in vitro* experiments on human fetal RPE, suggesting that an increase in apical and basal $CO_2$ enhances water transport. The motivation behind developing the current model is to better understand such processes.

The main objectives of the present modelling work are thus as follows. First, we examine the coupling between water and ion transport in the context of the RPE. Second, we consider the impact of $CO_2$, $HCO_3^-$, pH and $H_2CO_3$ on water transport, including alterations of the balance between the species via CA inhibition. Finally, we explore the effects of ion channel regulation on water transport.

## 2. Methods

### 2.1. Model set-up

We represent the RPE cell layer as a row of rectangles with length $L$ and width $H$ in a two-dimensional space (figure 2). The cells (denoted with superscript $i$ for intracellular; see table 1) are separated by a region of thickness $2h$, representing the cleft gap ($g$) and connected with tight junctions (tj). Above the cell layer there is the apical region ($a$), which is the SRS. The RPE sits on Bruch's membrane, and below this is the basal region ($b$), which is the choroid.

The apical membrane is assumed to be folded, leading to an area increase of a factor of 10 [1], which we neglect in the geometry but account for in the values of membrane permeability to water and uncharged solute. We introduce a Cartesian system of coordinates $(x, y)$, so that $x$ spans the length of the cleft and $x = 0$ corresponds to Bruch's membrane (figure 2).

We make the assumption that the solutions are well mixed in the apical and basal regions. The solute concentrations in these spaces are fixed and we formulate a mathematical model for water and ion transport across the cell and the cleft gap. We consider the presence of seven species: $Na^+$, $K^+$, $Cl^-$, $HCO_3^-$, $CO_2$, $H_2CO_3$ and $H^+$.

$CO_2$ and $HCO_3^-$ are subject to chemical rearrangement via the following two reactions:

$$HCO_3^- + H^+ \underset{k_{-1}}{\overset{k_1}{\rightleftharpoons}} H_2CO_3 \underset{k_h}{\overset{k_d}{\rightleftharpoons}} CO_2 + H_2O. \tag{2.1}$$

The first reaction is the dissociation of $H_2CO_3$ into the ions $HCO_3^-$ and $H^+$; it is rapid and happens almost instantaneously. The second reaction is normally slow, but can be catalysed up to six orders of magnitude in speed by CA [8]. There are a number of isoforms of CA: CA II is found in the cytosol of the RPE [17], whereas CA IV and XIV are attached to the cell membranes and are active in the extracellular membranes [18,19]. In effect, the presence of CA activity can be considered to be ubiquitous. The rates of this reaction are reported in table 2.

Although the second step of reaction (2.1) involves the production and consumption of water, the resulting changes are insignificant compared with the total water present. Accordingly, the amount of water is considered to be fixed.

The concentrations of anions and cations do not balance in the cell; there is an excess of cations. This deficiency of measured anions

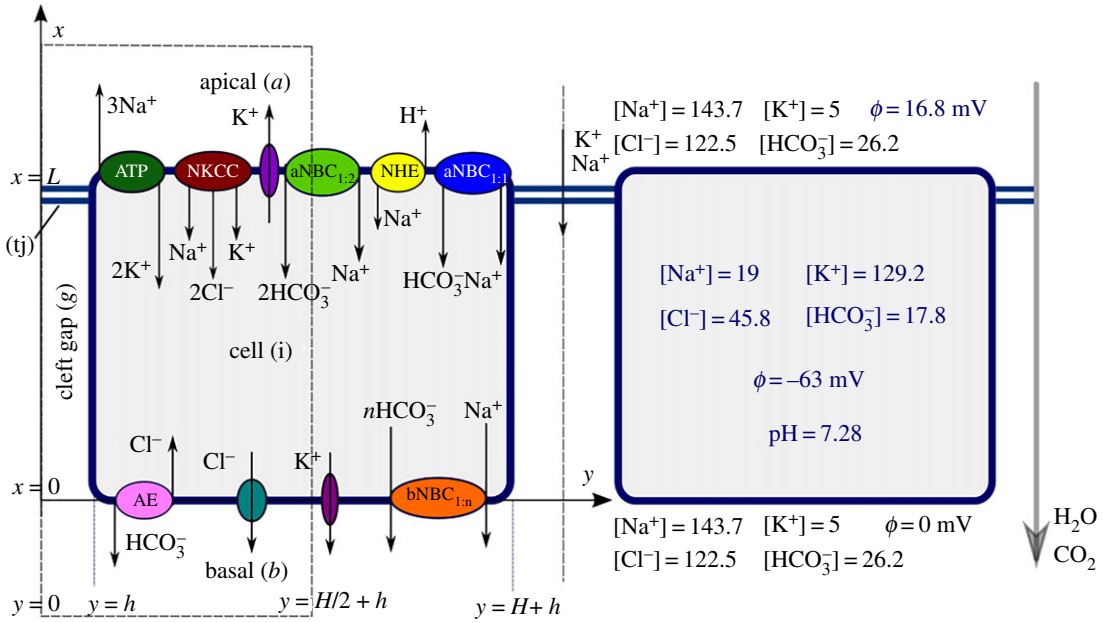


**Figure 2.** Left cell: Diagram of ion channels in the RPE cell membranes, with a sketch of the domain and coordinate system. Right cell: Typical values for species concentrations (in mM) and electrical potential (mV) under the open-circuit condition. The prescribed values are in black and the values predicted by the model are in blue for the reference parameters in table 2, with an identical concentration of $CO_2$ in the apical and basal regions. (Online version in colour.)

**Table 1.** List of notations and variables used in the model. Superscripts $s$ and $m$ denote generic regions from the set $\{a, b, g, i\}$. We highlight with a '*' the unknowns computed by the model in the regions reported in parenthesis. With '**' we denote the variables that are functions of the unknowns.

| | |
|---|---|
| $a, b, g, i$ | values of $s$ labelling apical, basal, cleft gap and intracellular regions, respectively |
| $n_k^s$, *$(i, g)$ | concentration of species $k$ in region $s$ (mM) such that $n_0^s = [Na^+]^s$, $n_1^s = [K^+]^s$, $n_2^s = [Cl^-]^s$, $n_3^s = [HCO_3^-]^s$, $n_4^s = [H^+]^s$, $n_5^s = [CO_2]^s$ and $n_6^s = [H_2CO_3]^s$ |
| $X$, *$(i)$ | concentration of non-diffusible anions in the cell (mM) |
| $B$, *$(i)$ and $HB$, ** | concentration of cytosolic and protonated buffer (mM) |
| $z_k$ | valence and charge of species $k$ |
| $f_k^s$, ** | kinetic description of reactions of species $k$ in region $s$ |
| $\phi^s$, *$(a, g, i)$ | electrical potential in region $s$ (V) |
| $\mathbf{j}_k^s$, ** | flux of species $k$ per unit area in region $s$ (mol m$^{-2}$ s$^{-1}$) |
| $J_k^{sm}$, ** | membrane flux of solute $k$ per unit area from region $s$ to region $m$ (mol m$^{-2}$ s$^{-1}$) |
| $Q^{sm}$, ** | water flux per unit area from region $s$ to region $m$ (m s$^{-1}$) |
| $\mathbf{u}$, ** | fluid velocity (m s$^{-1}$) |
| $p$, *$(g)$ | fluid pressure in the cleft gap (Pa) |

is called the anion gap and is due to some species not included in the model; in particular, both anions (such as lactate and phosphate) and non-diffusible proteins, which carry a net negative charge.

We model the anion gap by assuming the presence of a combination of two non-diffusible species. The first one, a buffer termed $B^-$, will react with $H^+$ within the physiological pH range and the reaction can be modelled as follows:

$$B^- + H^+ \underset{k_{-3}}{\overset{k_3}{\rightleftharpoons}} HB, \tag{2.2}$$

where HB is a protonated buffer, a product of the reaction (2.2), and is not charged. The total buffer concentration is fixed and conserved, and we denote it by $C_B := B + HB$, where $B$ and $HB$ denote the concentrations of $B^-$ and HB, respectively. We note that this representation of cytosolic buffering is highly simplified, representing a large number of different reactions.

The second group consists of non-diffusible molecules that are strong acids and do not react with $H^+$ in the physiological pH range. We denote their concentration by $X$ and the corresponding fixed negative charge by $\tilde{X} := z_X X$, where $z_X$ is the mean valence of these molecules. Therefore, the total concentration of fixed negative charge in the cell is $\tilde{X} + B$ and the total concentration of non-diffusible molecules is $X + C_B$.

The pumps, co-transporters and ion channels that we incorporate in the model are adapted from Adijanto *et al.* [1] and Reichhart & Strauß [20] (figure 2). A peculiar feature of the RPE cell is that the $Na^+/K^+$ ATPase is located in the apical membrane. It pumps three $Na^+$ out of the cell and two $K^+$ in (denoted in the following with subscript ATP). The apical membrane also has the NKCC co-transporter that transports $Na^+$, $K^+$ and two $Cl^-$ (NKCC), the $K^+$ channels, the electrogenic channel NBC1 that co-transports two $HCO_3^-$ and one $Na^+$ ($a$NBC$_{1:2}$) and the $Na^+/H^+$ exchanger (NHE) [21,22]. Following Adijanto *et al.* [1], we also account for the possible presence of the electroneutral $Na^+$–$HCO_3^-$ co-transporter ($a$NBC$_{1:1}$), where the $a$ stands for apical.

The basolateral membrane has $K^+$ channels, $Cl^-$ channels, the $HCO_3^-/Cl^-$ exchanger AE2 (AE) and the NBC channel that co-transports $Na^+$ and $HCO_3^-$. The stoichiometry of the NBC channel is not clear, with estimates varying from 1 : 2 ($Na^+ : 2HCO_3^-$) to 1 : 3 [1]. We have modelled this NBC channel as a combination of channels with stochiometry 1 : 2 ($b$NBC$_{1:2}$) and 1 : 3 ($b$NBC$_{1:3}$) in the basolateral membrane.

The tight junction is considered to be impermeable to anions [1].

We assume that both cell membranes are permeable to $CO_2$ and $H_2CO_3$, since these molecules are not polarized and can pass through the lipid bilayer. Water is transported across the membranes by aquaporins and we have attributed a given hydraulic conductivity to each membrane.

Throughout this paper, we adopt the notation presented in table 1 and the values reported in table 2 as the baseline. Unless stated otherwise, we use superscripts to label regions and subscripts to label species, which we number in the following way:

| $Na^+$ | $K^+$ | $Cl^-$ | $HCO_3^-$ | $H^+$ | $CO_2$ | $H_2CO_3$ |
|---|---|---|---|---|---|---|
| 0 | 1 | 2 | 3 | 4 | 5 | 6 |

We first present a spatially resolved model of solute transport with reactions. We then simplify the model using asymptotic expansions in terms of the aspect ratio of the cleft, $\delta = h/L$, and exploiting the fact that different time scales characterize reaction and diffusion processes. We then model fluid transport in the cleft. This model does not include electro-osmosis in the cleft, as it has been demonstrated to be subdominant [11], and instead focuses on water transport driven by osmosis. Finally, we impose water balance in the cell and describe the solution procedure.

## 2.2. Model of solute transport and water

Each ion $k \in \{0, 1, \ldots, 6\}$ is conserved in region $s \in \{i, g\}$

$$\frac{\partial n_k^s}{\partial t} = -\nabla \cdot \mathbf{j}_k^s + f_k^s, \tag{2.3a}$$

where $\nabla = (\partial/\partial x, \partial/\partial y)$, and is transported by electrodiffusion and advection [26]

$$\mathbf{j}_k^s = -D_k\left(\nabla n_k^s + \frac{z_k F}{RT} n_k^s \nabla \phi^s\right) + \mathbf{u} n_k^s. \tag{2.3b}$$

The anion gap is modelled to ensure electroneutrality,

$$\sum_{k=0}^{4} z_k n_k^s = X^s, \quad s \in \{i, g\}, \tag{2.3c}$$

where $X^i = z_X X + B$ and $X^g = 0$.

In the cell, we have an additional equation for the negatively charged cytosolic buffer (which we assume cannot diffuse),

$$\frac{\partial B}{\partial t} = f_{\mathrm{B}}^i. \tag{2.3d}$$

The concentration of HB can be found from the relation $HB = C_{\mathrm{B}} - B$. The $f_k^s$ are the reaction terms, modelled via the law of mass action [27] as follows:

$$\begin{aligned} f_3^s &= k_{-1} n_6^s - k_1 n_3^s n_4^s, \quad & f_{\mathrm{B}}^i &= k_{-3} HB - k_3 n_4^i B, \quad f_4^s = f_3^s + f_{\mathrm{B}}^s, \\ f_5^s &= -k_h n_5^s + k_d n_6^s, \quad & f_6^s &= -f_5^s - f_3^s, \quad s \in \{i, g\} \end{aligned} \tag{2.4}$$

with all other $f_k^s$ equal to zero.

We start simplifying our equations by comparing the time scales for reaction and diffusion processes. The time scale for diffusion in the cell is about $L^2/D \approx 0.06$ s, where $D = 1.7 \times 10^{-9}\ \mathrm{m^2\,s^{-1}}$ ($K^+$ in water, [28]) is a representative diffusion coefficient.

The time required for the first step of the reaction (2.1) and for the buffer reaction (2.2) is about $10^{-7}$ s. It thus makes sense to assume that the first step of the reaction (2.1) and the reaction (2.3*d*) are both effectively in equilibrium. This leads to the following relations:

$$n_6^s = K_d n_3^s n_4^s, \quad K_d = \frac{k_1}{k_{-1}}, \quad s \in \{i, g\} \tag{2.5a}$$

and

$$B = \frac{K_b C_{\mathrm{B}}}{K_b + n_4^i} \quad \text{and} \quad K_b = \frac{k_{-3}}{k_3}. \tag{2.5b}$$

We also note that the time scale for lateral diffusion in the cleft is much faster than in the cell, owing to its small width. Nevertheless, the relation (2.5*a*) still holds, as we prove in the electronic supplementary material.

In the second step of the reaction (2.1), catalysed hydration of $CO_2$ takes about $6 \times 10^{-4}$ s and dehydration $2 \times 10^{-6}$ s. These reaction rates are up to $10^6$ times slower in the absence of CA. As we are interested in studying the effect of CA inhibition, we do not assume that this step of the reaction (2.1) is in equilibrium [24].

We obtain an equation for total $CO_2$ conservation by considering (2.5*a*) and adding equations (2.3*a*) for $k = 3$, 5, 6 (bicarbonate, carbon dioxide and carbonic acid, respectively), resulting in

$$\frac{\partial n_3^s}{\partial t} + \frac{\partial n_5^s}{\partial t} + \frac{\partial n_6^s}{\partial t} = -(\nabla \cdot \mathbf{j}_3^s + \nabla \cdot \mathbf{j}_5^s + \nabla \cdot \mathbf{j}_6^s), s \in \{i, g\}. \tag{2.6}$$

We can further manipulate equations (2.3*a*) by subtracting equation (2.3*a*) for $k = 4$ from equation (2.3*a*) for $k = 3$ and adding (2.3*d*), to obtain the following relationship for conservation of charge:

$$\frac{\partial n_3^s}{\partial t} - \frac{\partial n_4^s}{\partial t} + \frac{\partial B}{\partial t} = -\nabla \cdot \mathbf{j}_3^s + \nabla \cdot \mathbf{j}_4^s, \quad s \in \{i, g\}. \tag{2.7}$$

We will be using equations (2.6) and (2.7) along with (2.5*a*) and (2.5*b*) instead of equations (2.3*a*) for $k = 3$, 4, 6 ($HCO_3^-$, $H^+$ and $H_2CO_3$, respectively) and (2.3*d*).

We do not explore transients (for example, the effects of transitioning from light to dark) and only focus on the steady-state behaviour of the system. Therefore, we have dropped all time derivatives.

### 2.2.1. Boundary conditions

We prescribe concentrations of solute in apical and basal regions $n_k^s$, $k \in \{0, \ldots, 6\}$, $s \in \{a, b\}$, as in table 2.

We impose at the membrane separating the generic regions $s$ and $m$ (either a cell membrane or a tight junction) the condition that the flux on the $s$ side of the membrane of species $k$ is equal to the function $J_k^{sm}$,

$$\mathbf{n}^{sm} \cdot \mathbf{j}_k^s = J_k^{sm}, \quad k \in \{0, \ldots, 6\}. \tag{2.8}$$

This describes both the passive and active flows of species $k$ across this membrane and the choice of the function is described in §2.2.2. Here, $\mathbf{n}^{sm}$ is the unit normal pointing from region $s$ to region $m$.

Without loss of generality, we impose the potential in the basal region (at the level of Bruch's membrane) to be zero. We prescribe Dirichlet conditions for all variables at the bottom of the cleft gap, $x = 0$ (which is also at the level of Bruch's membrane), so that

$$n_k^g = n_k^b, \quad \phi^g = 0, \quad k \in \{0, \ldots, 6\}. \tag{2.9a}$$

We also have symmetry conditions, at $y = 0$ and $y = H/2 + h$, which read

$$\frac{\partial \phi^s}{\partial y} = \frac{\partial n_k^s}{\partial y} = 0, \quad k \in \{0, \ldots, 6\}, \quad s \in \{i, g\}. \tag{2.9b}$$

Finally, we impose zero current at the apical region to simulate the open-circuit condition and to be able to compute the potential in the apical region ($\phi^a$)

$$\int_h^{H/2+h} \sum_{k=0}^{4} z_k \mathbf{j}_k^i \cdot \mathbf{n}^{ia}\, \mathrm{d}y + \int_0^h \sum_{k=0}^{4} z_k \mathbf{j}_k^g \cdot \mathbf{n}^{ga}\, \mathrm{d}y = 0, \quad \text{at } x = L. \tag{2.9c}$$

A schematic of boundary conditions is shown in figure 3. The problem in the cell and cleft is simplified to a set of ODEs along the $x$-axis in both cell and cleft (see the electronic supplementary material for the derivation) with an error of approximation

**Table 2.** Model reference parameters; please refer to the text for further details on their motivation. The detailed choice of the parameters is described in the electronic supplementary material.

| parameter | value | source |
|---|---|---|
| *geometry* | | |
| length of the cell, $L$ | 10 µm | [23] |
| height of the cell, $H$ | 10 µm | [23] |
| width of the cleft, $2h$ | 20 nm | |
| *thermodynamics* | | |
| ideal gas constant, $R$ | 8.314 J $K^{-1}$ $mol^{-1}$ | |
| temperature, $T$ | 310 K | |
| Faraday constant, $F$ | 96 485 C $mol^{-1}$ | |
| *membrane transport* | | |
| factor of apical membrane folding, $A_a$ | 10 | [1] |
| average valence of fixed negative charge in the cell, $z_X$ | 1.5 eq $mol^{-1}$ | |
| total concentration of intracellular buffer, $C_B$ | 60 mM | |
| representative diffusion coefficient, $D$ | $1.7 \times 10^{-9}$ $m^2$ $s^{-1}$ | |
| representative species concentration, $N$ | 100 mM | |

**pump, co-transporter and antiporter coefficients, mol $s^{-1}$ $m^{-2}$**

| $P_{ATP}$ | $P_{NKCC}$ | $P_{aNBC_{1:2}}$ | $P_{aNBC_{1:1}}$ | $P_{NHE}$ | $P_{AE}$ | $P_{bNBC_{1:2}}$ | $P_{bNBC_{1:3}}$ |
|---|---|---|---|---|---|---|---|
| $1.77 \times 10^{-6}$ | $1.78 \times 10^{-6}$ | $5.62 \times 10^{-7}$ | $10^{-7}$ | $3.16 \times 10^{-7}$ | $5.62 \times 10^{-7}$ | $5.62 \times 10^{-7}$ | $10^{-7}$ |

**valence $z_k$, diffusion coefficient $D_k$, permeability of membrane $s$, $P_k^s$ of species $k$**

| molecule | $Na^+$ | $K^+$ | $Cl^-$ | $HCO_3^-$ | $H^+$ | $CO_2$ | $H_2CO_3$ |
|---|---|---|---|---|---|---|---|
| $k$ | 0 | 1 | 2 | 3 | 4 | 5 | 6 |
| $z_k$ | +1 | +1 | −1 | −1 | +1 | 0 | 0 |
| $D_k$, $10^{-9}$ $m^2$ $s^{-1}$ | 1.7 | 1.7 | 1.7 | 1.23 | 9.69 | 1.5 | 1.5 |
| $P_k^a$, m $s^{-1}$ | 0 | $2.23 \times 10^{-7}$ | 0 | 0 | 0 | 0.015 | $1.28 \times 10^{-4}$ |
| $P_k^b$, m $s^{-1}$ | 0 | $3.16 \times 10^{-8}$ | $1.25 \times 10^{-8}$ | 0 | 0 | 0.0015 | $1.28 \times 10^{-5}$ |
| $P_k^{tj}$, m $s^{-1}$ | $10^{-5}$ | $10^{-5}$ | 0 | 0 | 0 | 0.015 | $1.28 \times 10^{-4}$ |
| $n_k^s$, $s = a, b$, mM | 143.7 | 5 | 122.5 | 26.2 | pH = 7.45 | 1.7 | 0.005 |

| parameter | value | source |
|---|---|---|
| *reaction rates* | | |
| hydration of $CO_2$ (catalysed), $k_h$ | $1.45 \times 10^3$ $s^{-1}$ | [24] |
| dehydration of $CO_2$ (catalysed), $k_d$ | $4.96 \times 10^5$ $s^{-1}$ | |
| equilibrium constant of $H_2CO_3$ dissociation, $K_d = k_1/k_{-1}$ | 5.3 $mM^{-1}$ | [1] |
| equilibrium constant of buffering reaction, $K_b = k_{-3}/k_3$ | $1.7 \times 10^{-4}$ mM | |
| *fluid dynamics* | | |
| hydrodynamic permeability of the membrane, $k$ | $1.28 \times 10^{-12}$ m $s^{-1}$ $Pa^{-1}$ | [25] |
| hydrodynamic permeability of the tight junction, $k^{tj}$ | $1.28 \times 10^{-10}$ m $s^{-1}$ $Pa^{-1}$ | |
| dynamic viscosity, $\mu$ | $0.75 \times 10^{-3}$ Pa $s^{-1}$ | water at 35°C |

of order $\delta = h/L \approx 10^{-3}$. The resulting system of equations is summarized in electronic supplementary material, §§1 and 2.

### 2.2.2. Ion fluxes through cell membranes and tight junctions

There are two main pathways for fluid and solutes to cross the RPE. These are the transcellular pathway (where the transported material passes through the cell) and the paracellular pathway (where the material crosses the tight junctions and then passes down the cleft). The flux through cell membranes and the tight junctions of solute $k$ that accounts for all active and passive transport from region $m$ to region $s$ is in general given by the following expression:

$$J_k^{ms} = \mathcal{J}_k^{ms} + \mathcal{A}_k^{ms} + \sum_{l=0}^{6} \sum_{\alpha \in \mathscr{C}^{ms}} s_{lk}^{\alpha} P_{\alpha} \Delta \bar{\mu}_l^{ms}. \tag{2.10}$$

We note that $J_k^{ms} = -J_k^{sm}$. The first term in (2.10) accounts for passive flux of solute through the membrane. In the case of ions,

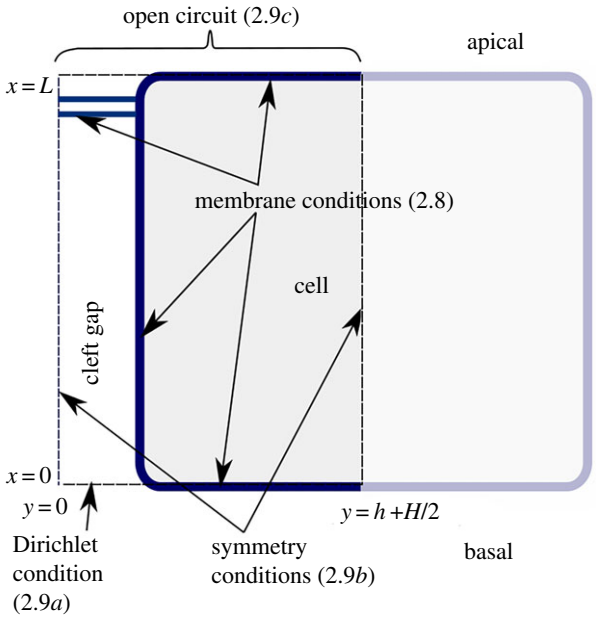


**Figure 3.** Sketch of the imposed boundary conditions. (Online version in colour.)

the passive flux through ion channels is modelled with the Goldman–Hodgkin–Katz expression [27],

$$\mathscr{J}_k^{ms} = P_k^s V_k^{ms} \frac{n_k^m - n_k^s \exp(-V_k^{ms})}{1 - \exp(-V_k^{ms})}, \qquad k \in \{0, \ldots, 4\}, \tag{2.11}$$

where $V_k^{ms} = (z_k F)/(RT)(\phi^m - \phi^s)$ and $P_k^s$ is the permeability of membrane $s$ to ion $k$. We refer the reader to tables 1 and 2 for the meaning of other symbols and values of the constants in this expression. We model the flux of $CO_2$ and $H_2CO_3$ across the cell membranes with the following expressions:

$$\mathscr{J}_k^{ms} = P_k^s (n_k^m - n_k^s), \quad k \in \{5, 6\}. \tag{2.12}$$

The second term in (2.10), $\mathscr{A}_k^{ms}$, accounts for the active transport, which in the case of RPE is due to the presence of $Na^+/K^+$ ATPase in the apical membrane. We take the flux through this channel to be represented by the following expression [29]:

$$\mathscr{J}_{\mathrm{ATP}} = P_{\mathrm{ATP}} \left(\frac{n_0^i}{K_{\mathrm{Na}} + n_0^i}\right)^3 \left(\frac{n_1^a}{K_{\mathrm{K}} + n_1^a}\right)^2, \tag{2.13}$$

where $P_{\mathrm{ATP}}$ is the parameter that determines maximum pump capacity and $K_{\mathrm{Na}} = 0.2(1 + n_1^i/(8.33\,\mathrm{mM}))\,\mathrm{mM}$ and $K_{\mathrm{K}} = 0.1(1 + n_0^a/(18.5\,\mathrm{mM}))\,\mathrm{mM}$ are apparent $Na^+$ and $K^+$ dissociation constants. Therefore, the terms representing active transport for $Na^+$ and $K^+$ are $\mathscr{A}_0^{ia} = 3\mathscr{J}_{\mathrm{ATP}}$ and $\mathscr{A}_1^{ia} = -2\mathscr{J}_{\mathrm{ATP}}$, with the other $\mathscr{A}_k^{ms}$ equal to zero.

Finally, the last term in (2.10) represents fluxes through co-transporters and exchangers (excluding ATP), which are modelled using a linear non-equilibrium thermodynamics approach (similar to [8]). The set of such channels in the apical membrane is denoted by $\mathscr{C}^{ia} = \{a\mathrm{NBC}_{1:1}, a\mathrm{NBC}_{1:2}, \mathrm{NKCC}, \mathrm{NHE}\}$ and in the basolateral one by $\mathscr{C}^{ib} = \mathscr{C}^{ig} = \{\mathrm{AE}, b\mathrm{NBC}_{1:2}, b\mathrm{NBC}_{1:3}\}$ (with no such channels in the tight junctions). The inner sum in (2.10) is performed for all channels in $\mathscr{C}^{ms}$ for given regions $m$ and $s$. The factor $s_{lk}^{\alpha}$ is the product of the number of ions $l$ and $k$ in the stochiometry of channel $\alpha$, $\alpha \in \mathscr{C}^{ms}$. For each channel $\alpha$, this approach requires only one parameter to describe flux through this channel, $P_\alpha$, $\alpha \in \mathscr{C}^{ms}$, with the values reported in table 2. $\Delta\bar{\mu}_k^{sm}$ is the dimensionless chemical potential difference of ion $l$ between regions $m$ and $s$, $\Delta\bar{\mu}_l^{ms} = \ln(n_l^m/n_l^s) + V_l^{ms}$.

## 2.3. Fluid flow

Fluid flow in the cleft is governed by Stokes equations for incompressible flow,

$$-\nabla p + \mu \nabla^2 \mathbf{u} = 0 \tag{2.14a}$$

and

$$\nabla \cdot \mathbf{u} = 0, \tag{2.14b}$$

where $\mathbf{u} = (u, v)$ is fluid velocity, $p$ is pressure and $\mu$ is fluid dynamic viscosity. We use the fact that the equations have a gauge freedom in the pressure to assign zero pressure in the cell, $p^i = 0$. Following the experimental evidence that the pressure jump across the RPE is negligible [30], we further assume it has values of zero in the apical and basal regions, $p^a = p^b = 0$, treating these regions as zero-dimensional compartments. Across cell membranes and tight junctions, there are osmotic and pressure driven fluxes, given by expressions

$$Q^{ag} = k^{\mathrm{tj}} \left( RT \sum_{k=0}^{6} (n_k^a - n_k^g(L)) + p(L) \right) \tag{2.15}$$

and

$$Q^{is} = k^s \left[ RT \left( \sum_{k=0}^{6} (n_k^i - n_k^s) + X + C_{\mathrm{B}} \right) - p^s \right], \quad s \in \{a, b, g\}, \tag{2.16}$$

where $k^b = k^g = k$, $k^a = A_f k$ and $p^g = p(x)$. Therefore, boundary conditions on the cell walls and tight junction of the cleft are $v(x, \pm h) = \mp Q^{ig}$ and $u(L, y) = Q^{ag}$. We also assume non-slip conditions for the longitudinal velocity at $y = \pm h$, $u(x, \pm h) = 0$ and impose zero pressure at the boundary with the basal region. We use lubrication theory to simplify the problem to an ODE for the pressure in the cleft (see electronic supplementary material, §3, for the derivation).

Finally, we impose water balance in the cell using the following relation:

$$\int_0^H Q^{ia}\,\mathrm{d}y + \int_0^H Q^{ib}\,\mathrm{d}y + 2\int_0^L Q^{ig}\,\mathrm{d}x = 0. \tag{2.17}$$

This balance is required for the volume of the cell to remain constant and it provides the equation to determine the concentration of large negatively charged molecules in the cell, $X$. We note that $X$ is related to concentration of ions in the cell through the electroneutrality condition (2.3$c$), providing an additional coupling between fluid and ion transport.

## 2.4. Summary of the model

The mathematical model described above has been formulated in two dimensions. We use asymptotic expansions with respect to the small aspect ratio of the cleft $\delta = h/L$ to simplify it to a one-dimensional problem in the $x$-direction (see electronic supplementary material for the derivation). The model has 20 variables, denoted with a '*' in table 1: concentration of all species in the cell ($s = i$) and the cleft ($s = g$) ($n_k^s(x)$, $k \in \{0, \ldots, 6\}$), electrical potential ($\phi^s(x)$), concentration of negatively charged molecules in the cell ($X$), intracellular buffer ($B(x)$), fluid pressure ($p(x)$) and transepithelial potential (TEP) ($\phi^a$). These variables are found from solving numerically (see electronic supplementary material for the details) the nonlinear system of seven algebraic equations along with the 13 ODEs summarized in table 3. All the simplified equations along with the boundary conditions, the solution procedure and methods are presented in electronic supplementary material, §4.

## 2.5. Sensitivity analysis

Parameter estimation is always challenging as some of the necessary values are reported in the literature while others have a range of values reported. Our chosen set of baseline parameters are presented in table 2, and we describe how the choices were made in electronic supplementary material, §6.

Owing to the large number of parameters, we wish to determine their relative importance on the model output, focusing on

**Table 3.** Summary of the model with references to equations in the main text in two-dimensional form (second column) and their simplified one-dimensional version in the electronic supplementary material (third column). The numbers in parentheses in the first column indicate the number of equations.

| equations | full model | simplified model |
|---|---|---|
| conservation of solute in the cell and the cleft (8) | (2.3*a*) for $k = 0, 1, 2, 5$ | (4-2a), (4-2b) |
| conservation of charge (2) | (2.7) | (4-2c) |
| conservation of total $CO_2$ (2) | (2.6) | (4-2d) |
| equilibrium of the reaction (2.2) and first part of (2.1) (3) | (2.5*a*), (2.5*b*) | (4-2e), (4-2f) |
| electroneutrality (2) | (2.3*c*) | (4-2g) |
| fluid transport (1) | derived from (2.14) | (4-2h) |
| water balance in the cell (1) | (2.17) | (4-2i) |
| open-circuit condition (1) | (2.9*c*) | (4-3g) |
| **boundary conditions at $x = 0$ and $x = L$** | | |
| imposed values at the exit of the cleft | (2.9) and $p(0) = 0$ | (4-3a) |
| membrane conditions | (2.8) | (4-3b)–(4-3e) |
| water flux across the tight junction | derived from $u(L, y) = Q^{ag}$ | (4-3f) |

**Table 4.** Parameters for the sensitivity analysis and their allowed ranges in the sensitivity study.

| membrane permeability | range, $10^8$ m s$^{-1}$ |
|---|---|
| $P_1^b$ - permeability of basal membrane to $K^+$ | [1, 10] |
| $P_1^a$ - permeability of apical membrane to $K^+$ | [10, 50] |
| $P_2^b$ - permeability of basal membrane to $Cl^-$ | [0.5, 3.16] |
| **amplitudes of ion channels** | **range, $10^6$ mol m$^{-2}$ s$^{-1}$** |
| $P_{ATP}$ - amplitude of the pump | [1, 3.16] |
| $P_{NKCC}$ - amplitude of co-transporter | [0.5, 5] |
| $P_{aNBC_{1:2}}$ - amplitude of apical $Na^+-HCO_3^-$ co-transporter | [0.1, 3.16] |
| $P_{aNBC_{1:1}}$ - amplitude of apical $Na^+-HCO_3^-$ electroneutral co-transporter | [0.01, 1] |
| $P_{bNBC_{1:2}}$ - amplitude of basal $Na^+-HCO_3^-$ co-transporter 1 : 2 | [0.1, 3.16] |
| $P_{bNBC_{1:3}}$ - amplitude of basal $Na^+-HCO_3^-$ co-transporter 1 : 3 | [0.01, 1] |
| $P_{AE}$ - amplitude of $Cl^--HCO_3^-$ exchanger | [0.1, 3.16] |
| $P_{NHE}$ - amplitude of $Na^+$–$H^+$ exchanger | [0.01, 10] |
| **tight junction permeability to cations** | **range, $10^6$ m s$^{-1}$** |
| $P^{tj}$ - permeability of tight junction to $Na^+$ and $K^+$ | [1, 100] |

their effect on water and ion fluxes. We accordingly perform global sensitivity analysis (GSA) using a variance-based method, known as the extended Fourier amplitude sensitivity test (eFAST), proposed in Saltelli *et al*. [31] and adapted to biological models in Marino *et al*. [32]. We consider the 12 parameters listed in table 4 and assume that their logarithms are uniformly distributed within given ranges, with the purpose of spanning several orders of magnitude. We further note that the qualitative results of the GSA are valid and, in conclusions reported below, are unchanged if the parameters are instead uniformly distributed across their range.

eFAST produces two sensitivity indices for each parameter: the first-order sensitivity index $S_i$ and the total sensitivity index $S_{Ti}$. $S_i$ describes the 'main effect' of each parameter and is a measure of the expected reduction in variance of the model output if that parameter were kept fixed. $S_{Ti}$ captures both this first-order effect and the interaction of a given parameter with other parameters. In other words, it measures the expected variance that would be left if all but a given parameter were fixed. These indices allow one to determine parameters which affect the model output most. A detailed meaning and definition of these indices can be found in Saltelli *et al*. [31]. In electronic supplementary material, §5, we report the particular choices we made for the implementation of the method.

## 3. Results

Photoreceptors have different levels of metabolic activity, varying with exposure to light: it is much higher in the dark. This means that in dark conditions $CO_2$ is produced in the SRS at a higher rate. We, therefore, focus on two physiologically relevant cases. In the first one, we impose the same values of $CO_2$ concentration in the apical and basal regions, representing retina exposed to light. We first show the results for the baseline parameter values reported in table 2 and then we provide the results of the sensitivity analysis. In the second case, we

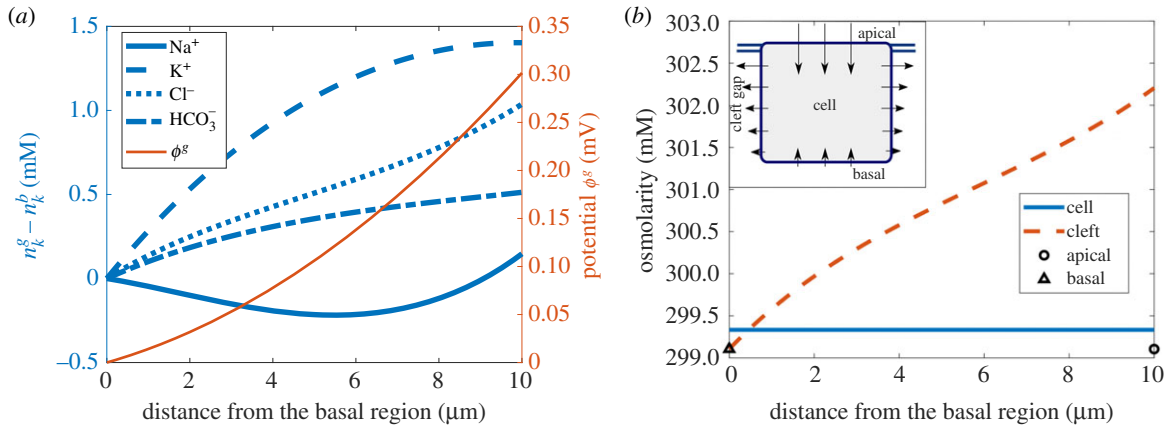


**Figure 4.** (*a*) Left axis: deviation of the ion concentrations along the cleft from those in the basal region for the reference parameters in table 2. The *x*-axis goes along the symmetry mid-line ($y = 0$) of the cleft, from the basal region to the tight junction. Right axis: electrical potential along the *x*-axis in the cleft. (*b*) Osmolarity distribution along the cell ($y = H/2 + h$) and cleft ($y = 0$). The osmolarities in the apical and basal regions are shown with a circle and a triangle, respectively. Inset: schematic of the direction and magnitude of water fluxes across cell membranes. (Online version in colour.)

consider a higher $CO_2$ concentration in the apical region than in the basal, representing retina in the dark.

## 3.1. Equal $CO_2$ concentration in the sub-retinal space and the choroid

In the absence of concentration jumps across the RPE the concentration of all species in the cell is constant. In figure 2 (right cell), we report the values of the concentrations and the electrical potential computed by the model. The concentrations predicted for $Na^+$, $K^+$ and TEP ($\phi^a$) compare well to experimentally measured values [12,20].

The measured values of the $Cl^-$ concentration vary across the literature, from 62 mM in the bovine RPE [33] to about 20 mM in the toad and chick RPE [34,35]. The value computed by the model is within this range, but we note that it is high compared with some other mammalian cell types. Nevertheless, the sensitivity analysis shows that this value does not significantly affect the behaviour of the system (results not reported).

$HCO_3^-$ concentration and pH predicted values are comparable to those reported in Gallemore *et al.* [36]. We note that, owing to the large permeability of cell membranes to $CO_2$ and $H_2CO_3$, their concentrations in the cell are predicted to be almost exactly the same as the values imposed in the apical and basal regions, i.e. $n_5^i = 1.7$ mM and $n_6^i = 0.49 \times 10^{-2}$ mM.

With the reference parameter set from table 2, the model predicts the following ion fluxes:

| | $Na^+$ | $K^+$ | $Cl^-$ | $HCO_3^-$ |
|---|---|---|---|---|
| ion flux, mol m$^{-2}$ s$^{-1}$ | $-1.44 \times 10^{-6}$ | $-1.69 \times 10^{-6}$ | $-2.34 \times 10^{-6}$ | $-7.79 \times 10^{-7}$ |

directed from the SRS to the choroid (corresponding to a negative value). Measurements of ion fluxes across the RPE are limited and incomplete, with different authors even finding fluxes in opposite directions. Our model predicts an $Na^+$ flux in agreement with the value of $-1.5 \times 10^{-6}$ mol m$^{-2}$ s$^{-1}$ measured in an isolated bullfrog RPE-choroid preparation [2]. The calculated $K^+$ and $Cl^-$ fluxes are comparable to those in Dvoriashyna *et al.* [11] and the predicted $HCO_3^-$ flux is smaller than that estimated by Hughes *et al.* [2], $-3.13 \times 10^{-6}$ mol m$^{-2}$ s$^{-1}$.

We also find that concentration gradients do form in the thin cleft gaps that separate adjacent cells, owing to the presence of active ion pumping, as shown in figure 4*a*. In this figure, we also show the electrical potential along the cleft gap. The potential gradient is positive, opposite to the prediction of Dvoriashyna *et al.* [11]. We attribute this to using a different value for the tight junction cation permeability. This change in value was required in order to obtain the experimentally observed values of TEP. This implies that the value of $\phi^g$ on approaching the apical region is closer to the TEP.

Figure 4*b* shows the osmolarity in the cell and the cleft predicted by the model. The osmolarity in the cleft is higher than that in the cell and this induces a local osmotic flux. The overall effect is the generation of a net water flux across the RPE, directed from the apical to the basal region. A schematic of water fluxes through the cell and the cleft is shown in the inset of figure 4*b*. For the reference parameters in table 2, we find a value of the water flux per unit surface across the RPE equal to $Q \approx -9.36 \times 10^{-9}$ m s$^{-1}$, which is comparable to measured values of $-[1.1, 2.8] \times 10^{-8}$ m s$^{-1}$ [3].

### 3.1.1. Global sensitivity analysis

We investigate the sensitivity of water and ion fluxes to the model parameters reported in table 4 with a GSA algorithm, eFAST. The first-order and total sensitivity indices of model parameters for water flux are shown in the histograms in figure 5. The height of each bar is a measure of how much the corresponding parameter affects water flux. Inspection of figure 5 shows that first-order and total indices lead to qualitatively similar results, identify the same parameters as being important for modifying water flux (the same is true for ion fluxes).

For the most significant parameters, we show in figure 6 scatter plots with the values of water flux, $Q$, taken in each numerical experiment versus the corresponding value of the parameter. In the plots, we also report in black a curve

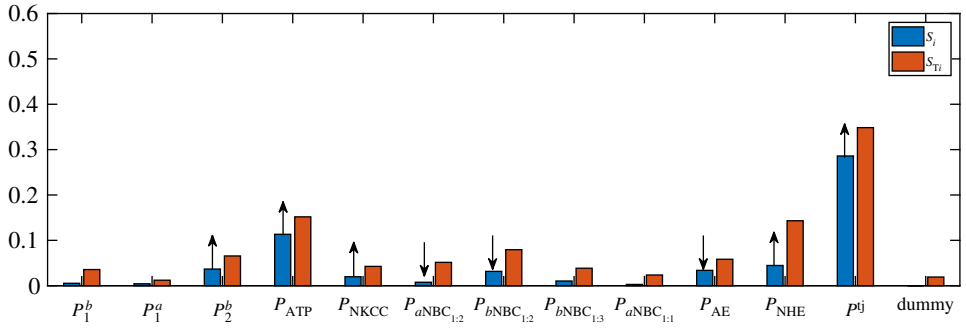


**Figure 5.** First and total sensitivity indices for water flux. For the large bars, arrows indicate how the magnitude of water flux is modified, up or down, by an increase in that particular parameter. The dummy parameter is introduced to verify the results: its deviation from zero can be interpreted as the uncertainty in the method, e.g. due to an insufficient number of points. (Online version in colour.)

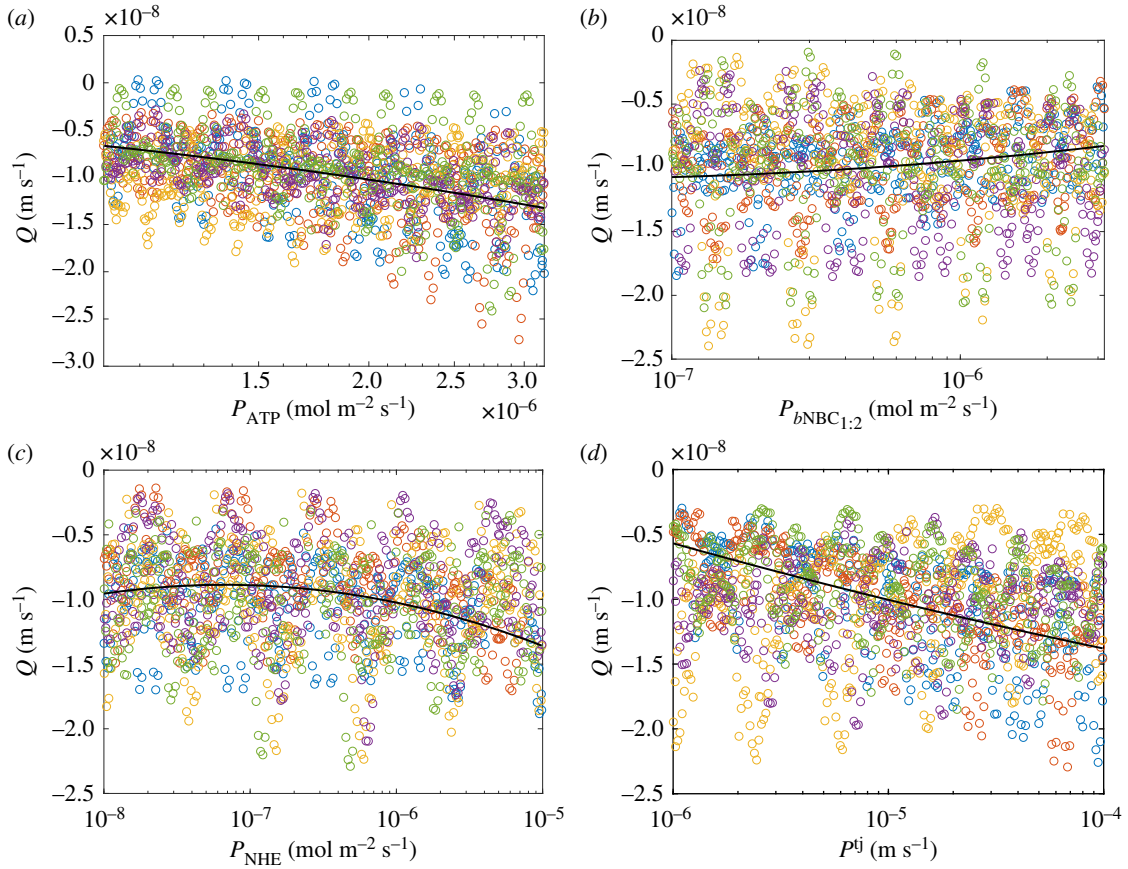


**Figure 6.** Scatter plots for water flux $Q$ versus four parameters with largest sensitivity indices: (*a*) $P_{ATP}$, (*b*) $P_{bNBC_{1:2}}$, (*c*) $P_{NHE}$ and (*d*) $P^{tj}$. Each point corresponds to a numerical experiment. Different colours correspond to different searching curves. (Online version in colour.)

corresponding to a second-order polynomial function fitted to the data with the least-squares method.

In figure 7, we report total sensitivity indices for ion fluxes. In the figure indices corresponding to different ions are reported with different colours. The sensitivity analysis for ion fluxes highlights the great importance that the $Na^+$–$H^+$ exchanger and the tight junction permeability have on the system.

It is believed that ion and water fluxes through epithelia are tightly linked to each other and that 'water follows the ions'. We examine this statement in figure 8, where we plot water flux versus each of the ion fluxes. Each point corresponds to a numerical experiment and we identify a general trend in each scatter plot by reporting (in black) a line fitted with the least-squares method. The figure shows that a strong link exists between water flux and $Na^+$ and $HCO_3^-$ fluxes. To a smaller extent, $Cl^-$ flux is also correlated with water flux. On the other hand, a clear correlation is not found for $K^+$ flux. The model does confirm that there is a link between ion and water fluxes, though it is not always conclusive and the concept that water follows the ions is not a general principle.

We simulated varying the $CO_2$ concentration on both sides of the epithelium from 1% to 13% and determined the predicted responses of water flux, following the experiments performed by Adijanto *et al.* [1]. Unlike in the experimental observations, our model does not predict any significant change in water transport with variation of $CO_2$ (results not shown).

## 3.2. Different $CO_2$ concentration in the sub-retinal space and the choroid

$CO_2$ is produced by photoreceptors at high rates in dark conditions. This results in a higher $CO_2$ concentration in the SRS

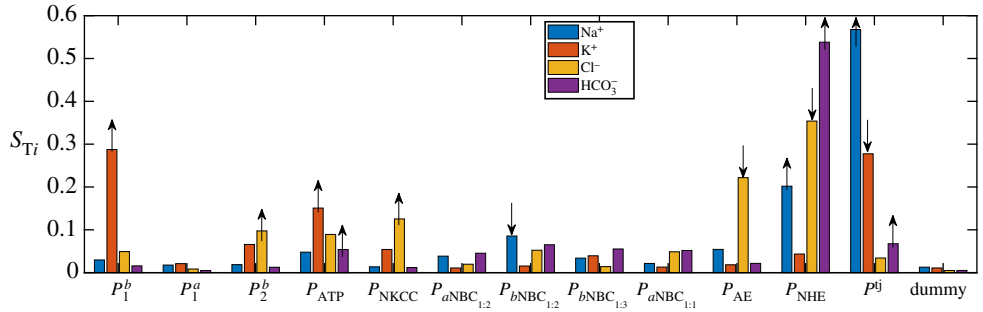


**Figure 7.** Total sensitivity index for ion fluxes. The arrows indicate the direction of ion flux change with the increase in a given parameter. (Online version in colour.)

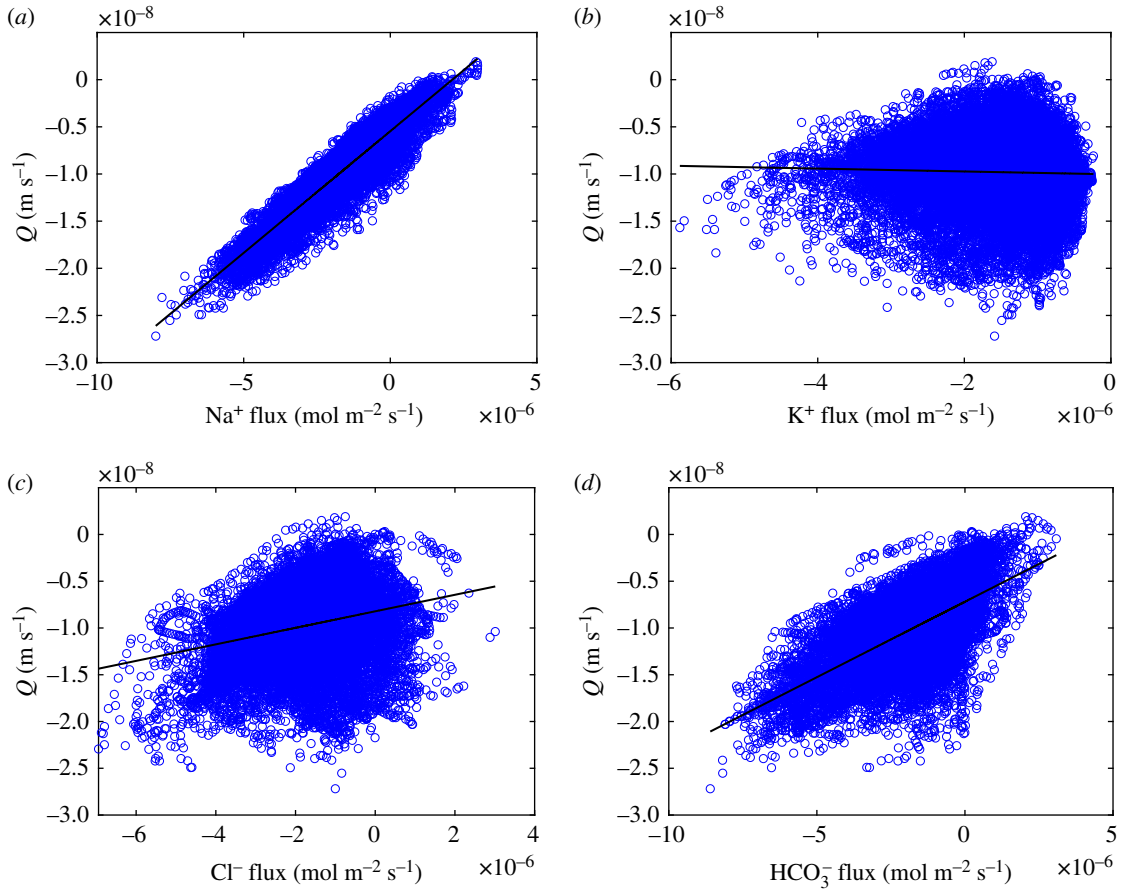


**Figure 8.** Scatter plots for water flux $Q$ versus (*a*) $Na^+$, (*b*) $K^+$, (*c*) $Cl^-$ and (*d*) $HCO_3^-$ flux. Each point corresponds to a numerical experiment. (Online version in colour.)

than in the choroid. To model this condition, we assume that $CO_2$ concentration in the basal region is fixed at 5% and we increase the concentration in the apical region to 7%. This creates a jump in $CO_2$ concentration across the RPE, which induces spatial variability of all variables in the $x$-direction in the cell. These induced departures of ion concentrations from the corresponding average values $\hat{n}_k^i$ along the cell are shown in figure 9*a*. While the average values are approximately the same as reported in figure 2, there is a concentration gradient, with the concentrations of $Na^+$ and $K^+$ decreasing towards the apical membrane, whereas concentrations of $Cl^-$ and $HCO_3^-$ increase. Moreover, figure 9*a* also shows that a potential gradient became established across the cell in a basal-to-apical direction.

Interestingly, despite these changes in the ion concentration and the potential gradients that were generated in the cell, there was little change in the net ion fluxes. This is because the concentration and the potential gradient act in opposite directions on the ion transport. With the established $CO_2$ gradient, there was a transepithelial $CO_2$ flux equal to $-9.05 \times 10^{-5}$ mol m$^{-2}$ s$^{-1}$, and directed from the apical to the basal region.

The osmolarity in the cell and a schematic of water fluxes across the cell membranes are shown in figure 9*b*. The decrease in osmolarity towards the apical membrane reduces the magnitude of the transepithelial water flux to the value of $-0.43 \times 10^{-8}$ m s$^{-1}$.

We also performed a GSA for the case with a $CO_2$ gradient but do not report these results since the conclusions are similar to those discussed above.

### 3.2.1. Impact of carbonic anhydrase inhibition

In order to test the effect of CA inhibition, we introduce a factor $\alpha$ that multiplies the reaction rates ($k_d$ and $k_h$) of equation (2.1)

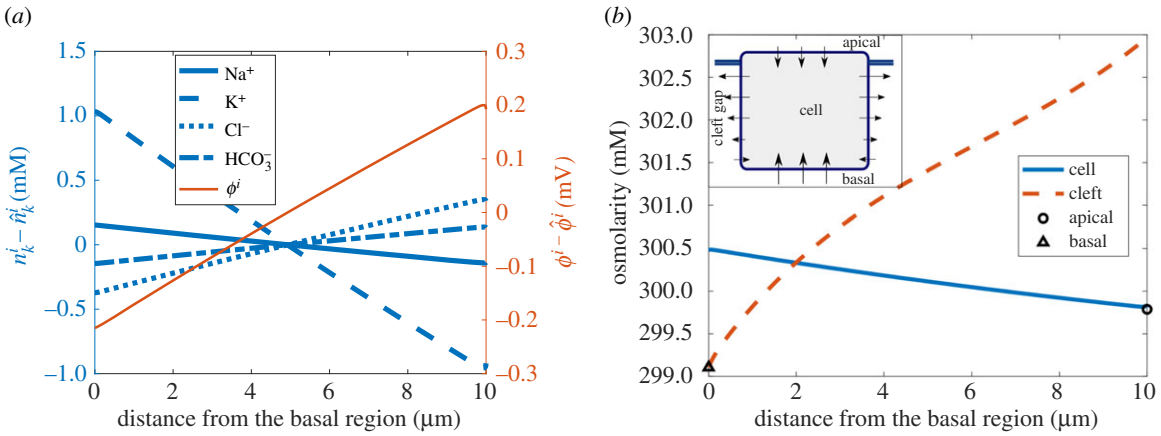


**Figure 9.** The case of apical $CO_2$ at 7% and basal $CO_2$ at 5%. (*a*) Left axis: deviation of ion concentrations from their average value in the cell along the *x*-axis, $\hat{n}_k^i = \int_0^L n_k^i \, dx/L$. Right axis: deviation of the electrical potential along the *x*-axis in the cell from its average value. (*b*) Osmolarity distribution in the cell, cleft, apical and basal regions. Inset: schematic of the direction and magnitude of water fluxes across cell membranes. (Online version in colour.)

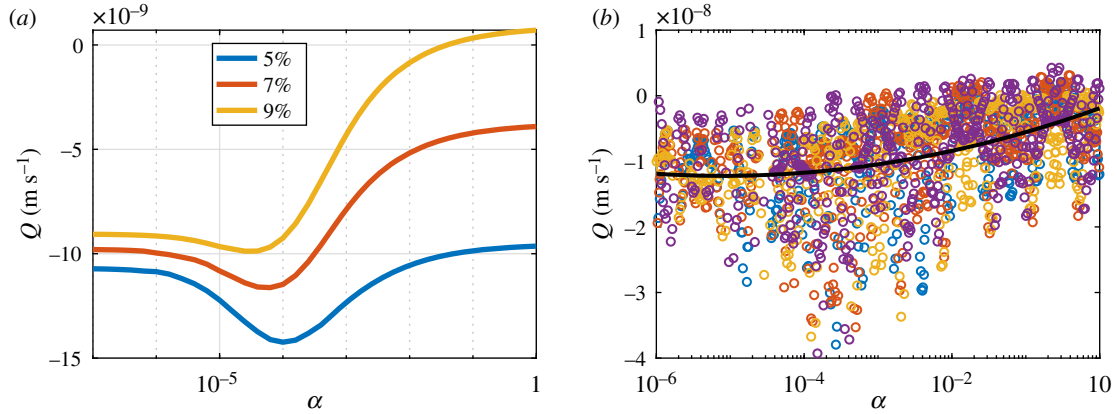


**Figure 10.** Water flux as a function of the CA activity. The values of $\alpha$ on the *x*-axes are factors that multiply the reaction rates $k_d$ and $k_h$ of the reaction (2.1). The value $\alpha = 1$ corresponds to full catalysis (the reaction rates from table 2); as the value of $\alpha$ decreases the catalyser is progressively inhibited. In (*a*), the typical solution, with other parameter values from table 2, is considered. Different curves correspond to different values of apical $CO_2$ concentration: 5%, 7% and 9%, while basal $CO_2$ is kept at 5%. In (*b*), we vary nine model parameters from table 4, keeping membrane permeabilities to ions ($P_1^b$, $P_1^a$ and $P_2^b$) fixed, while inhibiting CA with apical $CO_2$ at 7% and basal $CO_2$ at 5%. Different colours correspond to different searching curves. (Online version in colour.)

and their reduction simulates inhibition of this reaction. The response of water flux $Q$ to a progressive decrease of this factor is shown in figure 10*a*. The three curves correspond to three different $CO_2$ concentrations (5%, 7% and 9%) imposed in the apical region (the basal $CO_2$ concentration is kept fixed to 5%). The figure shows that inhibition of CA leads to a significant change in water flux towards the choroid. When a $CO_2$ drop across the RPE is imposed, water flux towards the choroid reduces. However, water flux increases significantly if reaction (2.1) is inhibited, especially when a $CO_2$ jump across the RPE is imposed. When $CO_2$ concentration is the same in the apical and basal regions the water flux reaches a maximum value for $\alpha \approx 10^{-4}$. The scatter plot in figure 10*b* shows the effect of CA inhibition on water flux $Q$ for various model parameters. The average behaviour suggests that $Q$ increases in magnitude with CA inhibition.

## 4. Discussion

Fluid accumulation in the SRS remains a relatively poorly understood problem, despite its clinical relevance for the formation and development of various sight-threatening pathological conditions, such as macular oedema, retinal detachment and age-related macular degeneration [37], and so a good understanding of this process is of considerable importance. Mathematical modelling has the potential to significantly contribute in this field by developing a framework that can help clarify underlying physical mechanisms and direct and interpret further experimental work.

In the present work, we develop a fully coupled, spatially resolved model of fluid and solute dynamics across the RPE and aim to study mechanisms of their interaction, extending the study of Dvoriashyna *et al*. [11]. We also perform a GSA to help identify which processes have the largest impact on transport.

The model predicts that ion concentrations in the cell and TEP are within physiological range. We also find that the concentration gradient in the cleft drives a water flux from the SRS to the choroid of the order of $10^{-8}$ m s$^{-1}$, which is compatible with the experimentally measured values of $[1.1,\ 2.8] \times 10^{-8}$ m s$^{-1}$ [2,3]. The predicted ion fluxes also have magnitudes comparable to those found experimentally [2,38,39].

The sensitivity results, from GSA, suggest that the tight junction plays a key role in $Na^+$ transport, and large tight junction permeability to cations is required for the $Na^+$ flux to be directed from the SRS to the choroid. This is in agreement

with the hypothesis of Gallemore *et al*. [37], who argued that the passive flux through the tight junction towards the choroid should exceed the active flux of $Na^+$ across the cell towards the SRS and establishes a net $Na^+$ transport towards the choroid. Our model also predicts that water flux is roughly proportional to $Na^+$ flux, with a proportionality constant of 0.0026 $m^3\ mol^{-1}$.

The $HCO_3^-$ flux is closely related to $Na^+$ transport, owing to their coupling through $Na^+-HCO_3^-$ co-transporters in cell membranes. Hughes *et al*. [2] performed experiments on isolated bullfrog RPE-choroid preparations that suggested that fluid absorption is strongly dependent on the active absorption of $HCO_3^-$. The results of our model agree with this, since our model predicts that water flux is roughly proportional to $HCO_3^-$ flux, and provides a proportionality constant of 0.0016 $m^3\ mol^{-1}$.

The GSA suggests that $Cl^-$ transport is directed in most cases towards the choroid. We note that the direction of this flux is obtained from a balance between basal $Cl^--HCO_3^-$ exchanger and basolateral permeability to $Cl^-$. Our model confirms the hypothesis that fluid transport is enhanced by a transepithelial $Cl^-$ flux (e.g. [33]), although the effect is less evident than that for $Na^+$ and $HCO_3^-$.

The GSA indicates which manipulations to perform in order to adjust the flow. In particular, the model predicts that increasing the tight junction permeability to cations will result in an increase of the transepithelial $Na^+$ flux, and thus of water flux, towards the choroid. To a smaller extent, inhibition of basal $Na^+-HCO_3^-$ (1 : 2) co-transporter and anion exchanger also increases the rate of fluid removal from the SRS. The effect of the anion exchanger on water flux has been confirmed experimentally by Iserovich *et al*. [40].

The model predicts that the water flux is also sensitive to the amplitudes of $Na^+-H^+$ exchanger (NHE) and $Na^+-K^+$ ATPase, inhibition of which results in a decrease in water flux towards the choroid. Therefore, we anticipate that a side effect of NHE inhibitors, such as amiloride, or reduced activity of $Na^+-K^+$ ATPase, e.g. due to low metabolic activity, may result in fluid accumulation.

The model also predicts that if $CO_2$ is being excessively produced in the SRS, then the water flux in the direction of the choroid reduces. This is because of the presence of spatial variability in ion concentration induced by a $CO_2$ gradient in the cell. This in turn implies a change in osmolarity from the basal to the apical region, such that the osmolarity in the cell decreases towards the apical membrane. As a result, the osmotic water flux across the apical membrane is reduced (or even reversed), resulting in an overall reduction in water flux towards the choroid. In other words, the model suggests that $CO_2$ accumulation in the SRS tends to decrease water transport. The implication is that acidosis and fluid accumulation in the SRS are predicted to be linked to each other, which is experimentally testable.

CA inhibitors are used to facilitate fluid transport [13,14] or to treat macular oedema [15,16]. This behaviour is captured by the model since we find that, in the case of a $CO_2$ gradient across the RPE, inhibition of CA smooths the gradients of all species in the cell (except for $CO_2$), resulting in an increase in water transport towards the choroid. Thus the model provides a possible explanation for the physical mechanism behind the functioning of CA inhibitors.

Adijanto *et al*. [1] studied the dependency of water flux on $CO_2$ concentration in the apical and basal solutions. The authors found that an increase in $CO_2$ concentration on both sides of the epithelium from 5% to 13% results in a doubling of water flux, suggesting that water transport is facilitated by $CO_2$. Our model suggests that water flux is independent of equal $CO_2$ concentration changes on both sides of the membrane, in disagreement with Adijanto *et al*. [1], which may also indicate that the model is incomplete and additional factors may contribute for large uniform increases in $CO_2$. However, owing to the high level of coupling among numerous contributions to overall transport, the addition of further factors would make it difficult to identify and assess their potential impact.

To summarize, we present a mathematical model that explains some of the features of fluid and solute transport across the RPE. It couples fluid, ion and $CO_2$ dynamics across the epithelium and shows that fluid transport can be driven by local osmosis in the cleft. The model provides possible explanations of the mechanisms behind the functioning of CA inhibitors used to treat fluid accumulation in the SRS. The results of the model, and particularly of the GSA, may be used in providing mechanism-based insight for targeting inhibition of other channels to treat pathological eye states associated with fluid transport across the RPE. We finally remark that the model is based on factors that are common to all absorptive or secretive epithelia and, therefore, can constitute a basic framework for the study of fluid flow across other tissues.

Data accessibility. The codes written to produce the results of this research are available at the Oxford University Research Archive (ORA) with the doi:10.5287/bodleian:6g4oazYNE.

Authors' contributions. All authors contributed to formulating the mathematical model. M.D. wrote the codes and carried out the calculations. All authors edited the manuscript and gave final approval for publication.

Competing interests. We declare we have no competing interests.

Funding. The work has been supported by the Macular Society and UK Fluid Networks, funded by EPSRC grant no. EP/NO32861/1. M.D. acknowledges the support of the Italian National Group for Mathematical Physics.

Acknowledgements. The authors thank Prof. F. Grillo for drawing figure 1. M.D. acknowledges the Department of Civil, Chemical and Environmental Engineering of the University of Genoa (Italy), where most of this work was undertaken.

## References

1. Adijanto J, Banzon T, Jalickee S, Wang NS, Miller SS. 2009 $CO_2$-induced ion and fluid transport in human retinal pigment epithelium. *J. Gen. Physiol.* **133**, 603–622. (doi:10.1085/jgp.200810169)
2. Hughes BA, Miller SS, Machen TE. 1984 Effects of cyclic AMP on fluid absorption and ion transport across frog retinal pigment epithelium. Measurements in the open-circuit state. *J. Gen. Physiol.* **83**, 875–899. (doi:10.1085/jgp.83.6.875)
3. Shi G, Maminishkis A, Banzon T, Jalickee S, Li R, Hammer J, Miller SS. 2008 Control of chemokine gradients by the retinal pigment epithelium. *Invest. Ophthalmol. Vis. Sci.* **49**, 4620–4630. (doi:10.1167/iovs.08-1816)
4. Marmor M. 1990 Control of subretinal fluid: experimental and clinical studies. *Eye* **4**, 340–344. (doi:10.1038/eye.1990.46)
5. Fischbarg J. 2003 On the mechanism of fluid transport across corneal endothelium and epithelia in general. *J. Exp. Zool. A Ecol. Genet. Physiol.* **300**, 30–40. (doi:10.1002/jez.a.10306)

6. Diamond JM, Bossert WH. 1967 Standing-gradient osmotic flow: a mechanism for coupling of water and solute transport in epithelia. *J. Gen. Physiol.* **50**, 2061–2083. (doi:10.1085/jgp.50.8.2061)
7. Gin E, Crampin EJ, Brown DA, Shuttleworth TJ, Yule DI, Sneyd J. 2007 A mathematical model of fluid secretion from a parotid acinar cell. *J. Theor. Biol.* **248**, 64–80. (doi:10.1016/j.jtbi.2007.04.021)
8. Krahn TA, Weinstein AM. 1996 Acid/base transport in a model of the proximal tubule brush border: impact of carbonic anhydrase. *Am. J. Physiol. Renal Physiol.* **270**, F344–F355. (doi:10.1152/ajprenal.1996.270.2.F344)
9. Weinstein A, Stephenson J. 1979 Electrolyte transport across a simple epithelium. steady-state and transient analysis. *Biophys. J.* **27**, 165–186. (doi:10.1016/S0006-3495(79)85209-1)
10. Weinstein AM, Stephenson JL. 1981 Models of coupled salt and water transport across leaky epithelia. *J. Gen. Physiol.* **60**, 1–20. (doi:10.1007/bf01870828)
11. Dvoriashyna M, Foss AJE, Gaffney EA, Jensen OE, Repetto R. 2018 Osmotic and electroosmotic fluid transport across the retinal pigment epithelium: a mathematical model. *J. Theor. Biol.* **456**, 233–248. (doi:10.1016/j.jtbi.2018.08.009)
12. Strauss O. 2011 The retinal pigment epithelium. See https://webvision.med.utah.edu/book/part-ii-anatomy-and-physiology-of-the-retina/the-retinal-pigment-epithelium.
13. Kita M, Marmor M. 1992 Retinal adhesive force in living rabbit, cat, and monkey eyes. Normative data and enhancement by mannitol and acetazolamide. *Invest. Ophthalmol. Vis. Sci.* **33**, 1879–1882.
14. Wolfensberger TJ, Chiang RK, Takeuchi A, Marmor MF. 2000 Inhibition of membrane-bound carbonic anhydrase enhances subretinal fluid absorption and retinal adhesiveness. *Graefes Arch. Clin. Exp. Ophthalmol.* **238**, 76–80. (doi:10.1007/s004170050013)
15. Cox SN, Hay E, Bird AC. 1988 Treatment of chronic macular edema with acetazolamide. *Arch. Ophthalmol.* **106**, 1190–1195. (doi:10.1001/archopht.1988.01060140350030)
16. Fishman GA, Gilbert LD, Fiscella RG, Kimura AE, Jampol LM. 1989 Acetazolamide for treatment of chronic macular edema in retinitis pigmentosa. *Arch. Ophthalmol.* **107**, 1445–1452. (doi:10.1001/archopht.1989.01070020519031)
17. Korte GE, Smith J. 1993 Carbonic anhydrase type II in regenerating retinal pigment epithelium. A histochemical study in the rabbit. *Experientia* **49**, 789–791. (doi:10.1007/BF01923549)
18. Nagelhus EA, Mathiisen TM, Bateman AC, Haug F-M, Ottersen OP, Grubb JH, Waheed A, Sly WS. 2005 Carbonic anhydrase XIV is enriched in specific membrane domains of retinal pigment epithelium, Müller cells, and astrocytes. *Proc. Natl Acad. Sci. USA* **102**, 8030–8035. (doi:10.1073/pnas.0503021102)
19. Wolfensberger TJ, Mahieu I, Jarvis-Evans J, Boulton M, Carter ND, Nógrádi A, Hollande E, Bird AC. 1994 Membrane-bound carbonic anhydrase in human retinal pigment epithelium. *Invest. Ophthalmol. Vis. Sci.* **35**, 3401–3407.
20. Reichhart N, Strauß O. 2014 Ion channels and transporters of the retinal pigment epithelium. *Exp. Eye. Res.* **126**, 27–37. (doi:10.1016/j.exer.2014.05.005)
21. Lin H, Kenyon E, Miller S. 1992 Na-dependent pHi regulatory mechanisms in native human retinal pigment epithelium. *Invest. Ophthalmol. Vis. Sci.* **33**, 3528–3538.
22. Lin H, Miller SS. 1991 pHi regulation in frog retinal pigment epithelium: two apical membrane mechanisms. *Am. J. Physiol. Cell Physiol.* **261**, C132–C142. (doi:10.1152/ajpcell.1991.261.1.C132)
23. Marmor M. 1998 Structure, function, and disease of the retinal pigment epithelium. In *The retinal pigment epithelium* (eds M Marmor, T Wolfensberger), pp. 3–12. New York, NY: Oxford University Press.
24. Weinstein AM. 2005 A mathematical model of rat distal convoluted tubule. II. Potassium secretion along the connecting segment. *Am. J. Physiol. Renal Physiol.* **289**, F721–F741. (doi:10.1152/ajprenal.00044.2005)
25. Mathias R, Wang H. 2005 Local osmosis and isotonic transport. *J. Membr. Biol.* **208**, 39–53. (doi:10.1007/s00232-005-0817-9)
26. Probstein RF. 2005 *Physicochemical hydrodynamics: an introduction*. New York, NY: John Wiley & Sons.
27. Keener JP, Sneyd J. 2009 *Mathematical physiology*, vol. 1. New York, NY: Springer-Verlag.
28. Miller SS, Steinberg RH, Oakley II B. 1978 The electrogenic sodium pump of the frog retinal pigment epithelium. *J. Membr. Biol.* **44**, 259–279. (doi:10.1007/BF01944224)
29. Strieter J, Stephenson JL, Palmer LG, Weinstein AM. 1990 Volume-activated chloride permeability can mediate cell volume regulation in a mathematical model of a tight epithelium. *J. Gen. Physiol.* **96**, 319–344. (doi:10.1085/jgp.96.2.319)
30. Emi K, Pederson JE, Toris CB. 1989 Hydrostatic pressure of the suprachoroidal space. *Invest. Ophthalmol. Vis. Sci.* **30**, 233–238.
31. Saltelli A, Tarantola S, Chan K-S. 1999 A quantitative model-independent method for global sensitivity analysis of model output. *Technometrics* **41**, 39–56. (doi:10.1080/00401706.1999.10485594)
32. Marino S, Hogue IB, Ray CJ, Kirschner DE. 2008 A methodology for performing global uncertainty and sensitivity analysis in systems biology. *J. Theor. Biol.* **254**, 178–196. (doi:10.1016/j.jtbi.2008.04.011)
33. Bialek S, Miller SS. 1994 $K^+$ and $Cl^-$ transport mechanisms in bovine pigment epithelium that could modulate subretinal space volume and composition. *J. Physiol.* **475**, 401–417. (doi:10.1113/jphysiol.1994.sp020081)
34. Fujii S, Gallemore R, Hughes BA, Steinberg R. 1992 Direct evidence for a basolateral membrane $Cl^-$ conductance in toad retinal pigment epithelium. *Am. J. Physiol. Cell Physiol.* **262**, C374–C383. (doi:10.1152/ajpcell.1992.262.2.C374)
35. Gallemore RP, Steinberg RH. 1989 Effects of DIDS on the chick retinal pigment epithelium. I. Membrane potentials, apparent resistances, and mechanisms. *J. Neurosci.* **9**, 1968–1976. (doi:10.1523/JNEUROSCI.09-06-01968.1989)
36. Gallemore RP, Hughes BA, Miller SS. 1997 Retinal pigment epithelial transport mechanisms and their contributions to the electroretinogram. *Prog. Retin. Eye Res.* **16**, 509–566. (doi:10.1016/S1350-9462(96)00037-7)
37. Hughes BA, Gallemore RP, Miller SS. 1998 Transport mechanisms in the retinal pigment epithelium. In *The retinal pigment epithelium* (eds M Marmor, T Wolfensberger), pp. 103–134. New York, NY: Oxford University Press.
38. La Cour M. 1992 $Cl^-$ transport in frog retinal pigment epithelium. *Exp. Eye. Res.* **54**, 921–931. (doi:10.1016/0014-4835(92)90156-M)
39. Miller SS, Edelman JL. 1990 Active ion transport pathways in the bovine retinal pigment epithelium. *J. Physiol. (Lond.)* **424**, 283. (doi:10.1113/jphysiol.1990.sp018067)
40. Iserovich P, Qin Q, Petrukhin K. 2011 DPOFA, a $Cl^-/HCO_3$-exchanger antagonist, stimulates fluid absorption across basolateral surface of the retinal pigment epithelium. *BMC Ophthalmol.* **11**, 33. (doi:10.1186/1471-2415-11-33)